GEO SA-BSAR Synchronization and MTI Algorithm Based on Direct Signal and Clutter Subspace

Chang Cui , Xichao Dong , *Member, IEEE*, and Zhiyang Chen , *Member, IEEE*

Abstract—Geosynchronous (GEO) spaceborne-airborne bistatic synthetic aperture radar, consisting of a GEO transmitter and an airborne multichannel receiver, is a potential moving target indication (MTI) system. However, such systems encounter synchronization challenges due to noncooperative transmission and reception. Besides, the inaccurate GEO orbital position for the MTI processor construction results in a low output signal-to-noise ratio (SNR) and reduced target detection probability. To address this, this article proposes a synchronization and MTI method based on direct signal and clutter subspace, which can enhance the output SNR for target detection even if the GEO orbital position is inaccurate. This method utilizes the direct signal to compensate for time and frequency synchronization errors. In addition, the residual error caused by the imprecise GEO orbit is estimated by approximating the clutter subspace. Next, a modified MTI processor is employed to suppress clutter and focus moving targets by using the residual error. Finally, the effectiveness of the proposed method is verified by numerical simulation experiments based on real IGSO orbital parameters.

Index Terms—Bistatic synthetic aperture radar (SAR), geosynchronous (GEO) SAR, moving target indicator (MTI), synchronization.

I. INTRODUCTION

THE geosynchronous spaceborne-airborne bistatic synthetic aperture radar (GEO SA-BSAR) is a radar system that uses a GEO SAR as an illuminator of opportunity and an airborne multichannel system to receive signals [1], [2]. It makes secondary use of the transmit signal of GEO SAR and decreases the receiver's slant range to improve the signal-to-noise ratio (SNR), expanding the application potential of GEO SAR in moving target indication (MTI) [3], [4]. Recently, GEO SA-BSAR MTI has attracted much attention [5]. Some studies

The authors are with the Chongqing Innovation Center, Beijing Institute of Technology, Chongqing 401120, China, also with the Chongqing Key Laboratory of Novel Civilian Radar, Chongqing 401120, China, and also with the School of Information and Electronics, Beijing Institute of Technology, Key Laboratory of Electronic and Information Technology in Satellite Navigation, Ministry of Education, Beijing Institute of Technology, Beijing 100081, China (e-mail: cuichang0329@foxmail.com; xcdong@foxmail.com; zychen12@163.com).

have concentrated on signal-processing challenges such as spectral ambiguity [6], spectral aliasing [7], [8], and space-variant Doppler parameters [9], [10]. Nevertheless, these studies neglect several non-ideal factors. For instance, a GEO SA-BSAR system has two independent clocks in the transmitter and receiver, leading to a synchronization issue [11].

Bistatic SAR systems need accurate time and frequency parameters of the transmitter and receiver for error calibration in synchronization processing. In cooperative systems, such information can be obtained from external common signals such as GNSS signals [12], [13], and a pre-established bidirectional communication link [14], [15], [16], [17]. However, such precise information cannot be accessed directly from the transmitter in noncooperative systems. Typically, in a SA-BSAR system, the transmitter is located much higher than its receiver. Thus, the aircraft is generally equipped with an upward-facing antenna to receive the satellite's transmitted signals directly, which are called direct signals [19]. Then, the synchronization for SA-BSAR systems is based on direct signals [18]. The direct-signal envelope and phase contain information about the relative frequency difference and the slant range. Thus, synchronization can be realized by simply separating the two accurately and compensating for the echo signal.

The slant range of the direct signal can be calculated from the position of the transmitter and receiver, which can be obtained from satellite ephemerides and aircraft transponders [19], [20]. The satellite ephemeris is determined by initially observing the satellite through either ground stations or GNSS. Three-dimensional (3-D) orbits are then calculated using kinematic and dynamical models. The kinematic orbiting method has low computational requirements but suffers from a large error. Thus, it is suitable for real-time orbit measurements [21]. On the other hand, the kinetic orbiting method has high measurement accuracy but requires enormous computational effort. Thus, it is only suitable for generating precise orbits by postprocessing (acquired after several days) [22]. For low-earth-orbit (LEO) satellites, GNSS can observe the entire orbit, providing a real-time 3-D positioning error of less than 10 cm [23], [24], and a postprocessed orbit accuracy of better than 4 cm [25]. Compared with an LEO satellite, a GEO SAR operates at a higher altitude than navigation satellites, which makes it difficult to be detected by GNSS. Its orbit is primarily monitored from the ground station. Because the altitude of GEO SAR is much larger than the earth's radius, the viewing angles between different ground stations have minimal variations. This fact results in a lower orbit determination accuracy of GEO SAR compared to LEO

satellites [26]. The imprecise orbit of GEO SAR makes it difficult to separate synchronization errors from the direct-signal slant range during synchronization processing, leading to residual errors.

Previous studies on LEO spaceborne-airborne bistatic SAR mainly focused on imaging and interferometry. These works tend to use post-processing precision orbits during synchronization processing [18] to avoid residual synchronization errors introduced by inaccurate orbits. Some works of literature [19], [27] study the synchronization method for the LEO bistatic SAR system with inaccurate satellite position. In these methods, the ephemeris of the LEO SAR is accurate and the satellite's position errors are caused by the unknown initial slant range and starting sampling time. Thus, they compensate for the residual synchronization error by searching the optimal initial slant range and starting sampling time. However, the accurate ephemeris is only obtained several days later for GEO SAR, losing its effectiveness in MTI application, particularly for safety services during emergencies. Thus, the traditional synchronization method cannot adapt to the GEO SA-BSAR system with inaccurate satellite ephemeris.

To solve the above problems, this article discusses the impacts of synchronization and orbital errors on GEO SA-BSAR MTI and subsequently presents a GEO SA-BSAR synchronization and MTI method based on direct signal and clutter subspace. First, the proposed method preprocesses the echo signal by using the direct signal to compensate for time and frequency synchronization errors. However, this preprocessing step may introduce residual error due to the inaccuracies of the GEO orbit. Then, an analytical relationship is derived between the clutter subspace and the aforementioned residual error. Afterward, a cost function is constructed to estimate the residual error. Finally, the estimated residual error is utilized to reconstruct the MTI processor for clutter suppression and motion target focusing. After the processing, a high output SNR can be achieved for target detection.

The rest of this article is organized as follows. Section II deduces the GEO SA-BSAR motion target signal model under synchronization and orbital errors. Furthermore, it analyzes how these nonideal factors impede MTI performance. Section III proposes the GEO SA-BSAR MTI method based on direct signal and clutter subspace. Section IV demonstrates the effectiveness of the proposed method using simulation experiments. Finally, Section V concludes this article.

II. MODELING AND ANALYSIS OF GEO SA-BSAR SIGNALS UNDER NONIDEAL FACTORS

The synchronization errors of bistatic radar include beam synchronization errors, time synchronization errors, and frequency synchronization errors. For the GEO SA-BSAR system, the GEO SAR has a coverage width of thousands of kilometers, which makes it easy to achieve beam synchronization. Both time and frequency synchronization errors are due to the difference between the receiver and transmitter's frequency sources and cannot be ignored in GEO SA-BSAR systems. This section presents the GEO SA-BSAR signal model, which includes time
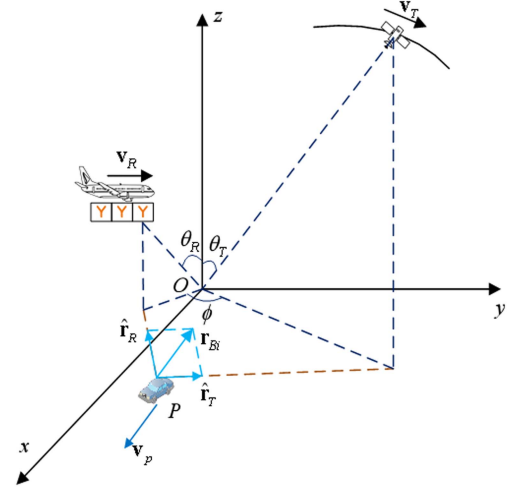

Fig. 1. GEO SA-BSAR moving target detection geometry schematic.

and frequency synchronization errors. It also analyzes the impact of synchronization and orbit errors on the MTI.

A. GEO SA-BSAR Signal Modeling

The GEO SA-BSAR MTI system is shown in Fig. 1, in which a multichannel receiver, mounted on an aircraft platform in side-looking mode, receives targets' reflected signals from the GEO SAR. An antenna installed on the top of the aircraft receives direct signals from the GEO SAR for synchronization.

Let the airborne receiver be located at $\mathbf{R}_0 = [x_{r0}, y_{r0}, z_{r0}]^T$ at the center of the aperture time and move along the y-axis with a uniform velocity v_R during the aperture time. The receiver has M channels, which are uniformly distributed along the flight direction and spaced d apart from neighboring channels. The GEO transmitter is located at $\mathbf{T}_0 = [x_t(t_a), y_t(t_a), z_t(t_a)]^T$ during the aperture time, where t_a is the slow time. Assume that a moving target with coordinates $\mathbf{P}_0 = [x_{p0}, y_{p0}, z_{p0}]^T$ in the scene is moving at a uniform speed during the aperture time with a velocity $\mathbf{v}_p = [v_{px}, v_{py}, v_{pz}]^T$. The slant range of the moving target at the mth receiver channel is denoted

$$R_{bi,m}\ (t_a) = R_{R,m}\ (t_a) + R_T\ (t_a) \tag{1}$$

where $R_{R,m}(t_a)$ is the slant range of the mth channel at the receiver and

$$R_{R,m}\ (t_a) = \sqrt{\begin{array}{c}[x_{r0} - x_{p0} - v_{px}t_a]^2 + [z_{r0} - z_{p0} - v_{pz}t_a]^2 \\ + [y_{r0} + m \cdot d + v_R t_a - y_{p0} - v_{py}t_a]^2\end{array}}$$
$$= \sqrt{v_{rel}^2(t_a - t_{0,m})^2 + R_{0,m}^2} \tag{2}$$

where

$$v_{rel} = \sqrt{v_{px}^2 + v_{pz}^2 + (v_{py} - v_R)^2} \tag{3}$$

$$t_{0,m} = t_0\ + \Delta t_{0,m} \tag{4}$$

$$R_{0,m} \approx R_0 + \Delta R_{0,m} \tag{5}$$

$$t_0 = \frac{v_{px}(-x_{p0}+x_{r0})+v_{pz}(-z_{p0}+z_{r0})}{v_{rel}^2} + \frac{(v_{py}-v_R)(-y_{p0}+y_{r0})}{v_{rel}^2} \tag{6}$$

$$\Delta t_{0,m} = \frac{d \cdot (m-1)(v_{py}-v_R)}{v_{rel}^2} \tag{7}$$

$$R_0 = \sqrt{\begin{array}{c}(x_{p0}-x_{r0})^2+(y_{p0}-y_{r0})^2\\+(z_{p0}-z_{r0})^2-v_{rel}^2 t_0^2\end{array}} \tag{8}$$

$$\Delta R_{0,m} \approx \frac{(-y_{p0}+y_{r0})-t_0(v_{py}-v_R)}{R_0}d\cdot(m-1). \tag{9}$$

$R_T(t_a)$ is the slant range from the target to the transmitter, and

$$R_T(t_a)$$
$$= \sqrt{\begin{array}{c}[x_t(t_a)-x_{p0}-v_{px}t_a]^2+[y_t(t_a)-y_{p0}-v_{pz}t_a]^2\\+[z_t(t_a)-z_{p0}-v_{pz}t_a]^2.\end{array}} \tag{10}$$

According to (1), (2) and (10), the bistatic slant range can be calculated. Then, the Taylor expansion of the bistatic slant range at $t = t_{0,m}$ is performed and retained up to the fourth-order term. The bistatic slant range model can be approximated as [9]

$$R_{bi,m}(t_a) \approx \alpha_0 + \alpha_1(t_a-t_{0,m}) + \alpha_2(t_a-t_{0,m})^2$$
$$+ \alpha_3(t_a-t_{0,m})^3 + \alpha_4(t_a-t_{0,m})^4 \tag{11}$$

where $\alpha_1 \sim \alpha_4$ is the first-order to fourth-order term coefficient of the bistatic slant range. Since the slant range is much larger than the channel spacing, $\alpha_1 \sim \alpha_4$ are approximately the same for different channels, and

$$\alpha_0 \approx R_0 + s_0 + \Delta R_{0,m} + s_1 t_{0,m} + s_2 t_0^2$$
$$\alpha_1 \approx s_1 + 2s_2 t_0$$
$$\alpha_2 \approx \frac{v_{rel}^2}{2R_0} + s_2$$
$$\alpha_4 \approx -\frac{v_{rel}^4}{8R_0^3}. \tag{12}$$

Then, the echo signal model of the mth channel can be expressed as

$$s_m(t_r,t_a) = \sigma w_r\left(t_r-\frac{R_{bi,m}(t_a)}{c}\right)\exp\left\{-j2\pi\frac{R_{bi,m}(t_a)}{\lambda}\right\}$$
$$w_a(t_a)\exp\left\{j\pi k_r\left(t_r-\frac{R_{bi,m}(t_a)}{c}\right)^2\right\} \tag{13}$$

where σ is the scattering coefficient of the target, t_r is the fast time, c is the speed of light, $w_r(\cdot)$ and $w_a(t_a)$ are the range and azimuth envelopes, respectively, k_r is the frequency rate, and λ is the radar wavelength.

Performing range compression and azimuth Fourier transform for the signal yields

$$z_m(t_r,f_a) = \sigma A W_a(f_a)\cdot\text{sinc}\left\{B_r\left[t_r-\frac{R(f_a)}{c}\right]\right\}.$$
$$\times\exp\{j\psi(f_a)\}$$

$$\exp\{-j2\pi f_a\Delta t_{0,m}\}\exp\left\{j\frac{2\pi}{\lambda}(\Delta R_{0,m}+s_1\Delta t_{0,m})\right\} \tag{14}$$

where $W_a(f_a)$ is the azimuth envelope in the frequency domain. $\psi(f_a)$ is the common phase term of the different channels and

$$\psi(f_a) = -\frac{2\pi}{\lambda}\alpha_0 - 2\pi f_a t_0 - \frac{\pi\lambda^2\alpha_3}{4\alpha_2^3}\left(f_a+\frac{\alpha_1}{\lambda}\right)^3$$
$$+ \frac{\pi\lambda}{2\alpha_2}\left(f_a+\frac{\alpha_1}{\lambda}\right)^2 - \frac{\pi\lambda^3\left(-9\alpha_3^2+4\alpha_2\alpha_4\right)}{32\alpha_2^5}\left(f_a+\frac{\alpha_1}{\lambda}\right)^4. \tag{15}$$

$R(f_a)$, as shown in (16), donates the range migration in the range-Doppler domain. The range migration between different channels does not exceed half a range resolution, so $R(f_a)$ can be approximately the same between different channels

$$R(f_a) = R_0 + s_0 + s_1 t_0 + s_2 t_0^2 - \frac{\alpha_1^2}{4\alpha_2} + \frac{\lambda^2}{4\alpha_2}f_a^2. \tag{16}$$

According to (14), the steering vector of the target in the range-Doppler domain is

$$\boldsymbol{p}_t(f_a) =$$
$$\begin{bmatrix}\exp\left\{-j\frac{2\pi}{\lambda}(\Delta R_{0,1}+s_1\Delta t_{0,1})\right\}\exp\{-j2\pi f_a\Delta t_{0,1}\}\\\vdots\\\exp\left\{-j\frac{2\pi}{\lambda}(\Delta R_{0,M}+s_1\Delta t_{0,M})\right\}\exp\{-j2\pi f_a\Delta t_{0,M}\}\end{bmatrix}. \tag{17}$$

B. GEO SA-BSAR Signal Model Including Synchronization Error

The multichannel signals all come from the same frequency source, and the synchronization error between different channels can be considered to be the same. Then, if echoes are not lost, the echo signal model with time and frequency synchronization errors of the mth channel for a target with an unknown position $(\mathbf{r}_p)$ and velocity parameters $(\boldsymbol{v}_p)$ can be expressed as

$$s_{e,m}(t_r,t_a) = s_m(t_r+e(t_a),t_a)\exp\{j2\pi f_c e(t_a)\}$$
$$\exp\{-j\Delta\varphi_{bi}(t_a)\} \tag{18}$$

where $e(t_a)$ is the time synchronization error and $\Delta\varphi_{bi}(t_a)$ is the phase introduced by frequency synchronization error. Due to the presence of the synchronization error, there is a time delay $e(t_a)$ in the echo signal, and phase errors $\exp\{j2\pi f_c e(t_a)\}$ and $\exp\{-j\Delta\varphi_{bi}(t_a)\}$ will be introduced after demodulating the received signal.

Literature [19] provides a detailed analysis of the modeling of the time error $e(t_a)$ and the phase error $\Delta\varphi_{bi}(t_a)$, where the time error $e(t_a)$ consists of a fixed time difference Δt_0, a linear error $\alpha\cdot t_a$ that accumulates with time, and a random time error $n_{prt}(t_a)$ that obeys a normal distribution

$$e(t_a) = \Delta t_0 + \alpha t_a + n_{prt}(t_a). \tag{19}$$

The phase difference $\Delta\varphi_{bi}(t_a)$ includes the phase error generated by the fixed frequency difference Δf_c, the smooth random phase error $\Delta\varphi_{st}(t_a)$, and the nonsmooth random phase error $\Delta\varphi_{rw}(t_a)$

$$\Delta\varphi_{bi}(t_a) = 2\pi\Delta f_c t_a + \Delta\varphi_{rw}(t_a) + \Delta\varphi_{st}(t_a). \tag{20}$$

The output signal model of the optimal processor will be derived to analyze the effect of synchronization error on the MTI. According to the synchronization error model, the phase errors $\exp\{j2\pi f_c e(t_a)\}$ and $\exp\{-j\Delta\varphi_{bi}(t_a)\}$ contain fixed phase error, linear error, and random error, where the linear phase error leads to additional Doppler shift. Thus, the signal model of the mth channel in the range-Doppler domain is denoted as

$$z_{e,m}\ (t_r, f_a) = z_m\ (t_r + e'\ (f_a), f_a - \Delta f)\exp\{j2\pi f_c\Delta t_0\}$$
$$\exp\{j\Delta\varphi_n\ (f_a)\} \tag{21}$$

where $e'(f_a)$ is the frequency domain expression of $e(t_a)$. $\Delta\varphi_n(f_a)$ is the phase noise in the frequency domain generated by random errors $n_{prt}(t_a)$, $\Delta\varphi_{rw}(t_a)$, and $\Delta\varphi_{st}(t_a)$. Δf is the Doppler shift generated by synchronization errors, which can be expressed as

$$\Delta f\ =\ \alpha f_c + \Delta f_c. \tag{22}$$

C. Impact of Synchronization and Orbit Errors on MTI

The purpose of MTI is mainly to detect a moving target and to estimate the motion parameters of the target [28]. In this section, the effects of synchronization and orbit errors on MTI are analyzed in terms of output SNR and parameter estimation.

In order to derive the output SNR, (21) is first expressed in the form of a vector

$$\boldsymbol{z}\ (t_r, f_a) =\ S\ (t_r, f_a)\,\boldsymbol{\Gamma}\boldsymbol{p}_t\ (f_a) \tag{23}$$

where $\boldsymbol{p}_t(f_a)$ is the target steering vector without error, $\boldsymbol{\Gamma}$ is the transformation matrix with synchronization error included, and $\boldsymbol{\Gamma}\boldsymbol{p}_t(f_a)$ is the target steering vector with synchronization error. $S(t_r, f_a)$ and $\boldsymbol{\Gamma}$ are expressed as

$$S\ (t_r, f_a) = \sigma A\text{sinc}\left\{B_r\left[t_r + e'\ (f_a - \Delta f) - \frac{R\ (f_a - \Delta f)}{c}\right]\right\}$$
$$W_a\ (f_a - \Delta f)\exp\{j2\pi f_c\Delta t_0\}$$
$$\exp\{j\psi\ (f_a - \Delta f)\}\exp\{j\Delta\varphi_n\ (f_a)\} \tag{24}$$
$$\boldsymbol{\Gamma}\ =\ \text{diag}\{\exp\ (j2\pi\Delta t_{0,1}\Delta f),\ldots,\exp\ (j2\pi\Delta t_{0,M}\Delta f)\} \tag{25}$$

It can be found that the synchronization error produces a Doppler shift Δf that results in a change in the steering vector. Setting the target velocity to 0 gives the stationary clutter range-Doppler-domain signal of the reference channel as $S_c(t_r, f_a)$ and the clutter steering vector as $\boldsymbol{p}_c(f_a)$. The multichannel range-Doppler-domain signal of the stationary target, then, can be expressed as

$$\boldsymbol{z}_c\ (t_r, f_a) = S_c\ (t_r, f_a)\,\boldsymbol{\Gamma}\boldsymbol{p}_c\ (f_a). \tag{26}$$

The covariance matrix of the clutter under the influence of time and frequency synchronization errors is denoted as

$$\boldsymbol{R_Q}\ (f_a) =\ E\left[\boldsymbol{z}_c\ (f_a)\,\boldsymbol{z}_c^H\ (f_a)\right]$$
$$=\ E\left[S\ (f_a)\,S^*\ (f_a)\right]\boldsymbol{\Gamma}\boldsymbol{p}_c\ (f_a)\,\boldsymbol{p}_c^H\ (f_a)\,\boldsymbol{\Gamma}^H + \boldsymbol{R_N} \tag{27}$$

where $\boldsymbol{R_N}$ is the covariance matrix of the noise, assumed to satisfy $\boldsymbol{R_N} = \sigma_n^2\,\boldsymbol{I}$. The analytic expression for the inverse of the clutter covariance matrix is obtained as (28) by derivation using matrix inversion lemmas

$$\boldsymbol{R_Q^{-1}}\ (f_a) = \frac{1}{\sigma_n^2}$$
$$\times\left[\boldsymbol{I} - \frac{E\left[S_c\ (f_a)\,S_c^*\ (f_a)\right]}{\sigma_n^2 + M\cdot E\left[S_c\ (f_a)\,S_c^*\ (f_a)\right]}\boldsymbol{\Gamma}\boldsymbol{p}_c\ (f_a)\,\boldsymbol{p}_c^H\ (f_a)\,\boldsymbol{\Gamma}^H\right]. \tag{28}$$

Then, the MTI processor can be constructed as

$$\boldsymbol{w}\ (f_a; \hat{\boldsymbol{v}}_p) = \frac{\boldsymbol{R_Q^{-1}}\ (f_a)\,\hat{\boldsymbol{p}}_t\ (f_a; \hat{\boldsymbol{v}}_p)}{\hat{\boldsymbol{p}}_t^H\ (f_a; \hat{\boldsymbol{v}}_p)\,\boldsymbol{R_Q^{-1}}\ (f_a)\,\hat{\boldsymbol{p}}_t\ (f_a; \hat{\boldsymbol{v}}_p)}. \tag{29}$$

$\hat{\boldsymbol{p}}_t(f_a; \hat{\boldsymbol{v}}_p)$ is an artificially constructed motion target steering vector based on (17) and the preset velocity $\hat{\boldsymbol{v}}_p$. Due to the inaccurate GEO orbit, it results in s_1 not being accurately calculated. Therefore, the relationship between $\hat{\boldsymbol{p}}_t(f_a; \hat{\boldsymbol{v}}_p)$ and $\boldsymbol{p}_t(f_a; \hat{\boldsymbol{v}}_p)$ is

$$\hat{\boldsymbol{p}}_t\ (f_a; \hat{\boldsymbol{v}}_p) = \boldsymbol{\Gamma}_{\text{GEO}}\,\boldsymbol{p}_t\ (f_a; \hat{\boldsymbol{v}}_p). \tag{30}$$

$\boldsymbol{\Gamma}_{\text{GEO}}$ is the error matrix resulting from the GEO orbital position error, which can be expressed as

$$\boldsymbol{\Gamma}_{\text{GEO}} =$$
$$\text{diag}\left\{\exp\left(-j2\pi\frac{\Delta s_1}{\lambda}\Delta t_{0,1}\right),\ldots,\exp\left(-j2\pi\frac{\Delta s_1}{\lambda}\Delta t_{0,M}\right)\right\} \tag{31}$$

where Δs_1 is the s_1 computational error generated by the GEO position error. At this point, the output response to a target signal with a velocity of $\boldsymbol{v}_p$ can be expressed as

$$y_e\ (t_r, f_a; \hat{\boldsymbol{v}}_p) =\ \boldsymbol{w}_{opt}^H\ (f_a; \hat{\boldsymbol{v}}_p)\,S\ (t_r, f_a)\,\boldsymbol{\Gamma}\boldsymbol{p}_t\ (f_a; \boldsymbol{v}_p)$$
$$=\ \frac{S\ (t_r, f_a)\,e^{j\frac{(A_1+A_2)(M-1)}{2}}}{M - \csc^2\left(\frac{A_1}{2}\right)\sin^2\left(\frac{A_1 M}{2}\right)}$$
$$\cdot\left(\frac{\sin\left[\frac{(A_1+A_2)M}{2}\right]}{\sin\left[\frac{(A_1+A_2)}{2}\right]} - \frac{\sin\left(\frac{A_1 M}{2}\right)\sin\left(\frac{A_2 M}{2}\right)}{\sin\left(\frac{A_1}{2}\right)\sin\left(\frac{A_2}{2}\right)}\right) \tag{32}$$

where

$$A_1 = \frac{2\pi}{\lambda}\,\Delta\hat{R}_{0,1} + 2\pi\left(f_a + \frac{\hat{s}_1}{\lambda}\right)\Delta\hat{t}_{0,1}$$
$$- \frac{2\pi}{v_R}d\left(f_a + \Delta f - \frac{s_{1,c}}{\lambda}\right) \tag{33}$$
$$A_2 = -\frac{2\pi}{\lambda}\Delta R_{0,1} - 2\pi\left(f_a - \Delta f + \frac{s_1}{\lambda}\right)\Delta t_{0,1}$$
$$+ \frac{2\pi}{v_R}d\left(f_a + \Delta f - \frac{s_{1,c}}{\lambda}\right) \tag{34}$$

where $\Delta\hat{R}_{01}$ and $\Delta\hat{t}_{01}$ are ΔR_{01} and Δt_{01} calculated from the assumed target velocity $\hat{\boldsymbol{v}}_p$ using (7) and (9), respectively. When there is no synchronization error, GEO position error, and assuming that the target velocity is the same as its true velocity,

there is $\Delta f = 0$, $\hat{s}_1 = s_1$, $\Delta \hat{R}_{01} = \Delta R_{01}$, $\Delta \hat{t}_{01} = \Delta t_{01}$, then $A_1 = -A_2$. So, the output response (32) is $y_e(t_r, f_a; \mathbf{v}_p) = S(t_r, f_a)$, that is to say, the output response is consistent with the reference channel motion target signal. When errors exist and the target velocity is assumed to be different from its true velocity, $A_1 \neq -A_2$. At this point, the output response changes the envelope of $S(t_r, f_a)$ and introduces a phase term with respect to f_a. The variation of the envelope, which is determined by A_1 and A_2, is related to synchronization errors, GEO orbit errors, and parameter estimation biases, and the variation of this envelope may produce an expansion of the target energy, leading to a decrease in the SNR.

Furthermore, the additional introduction of a phase term is determined by $A_1 + A_2$, producing a constant phase and a linear phase about f_a. This linear phase is associated with parameter estimation bias.

Finally, the output response $y_e(t_r, f_a; \hat{\boldsymbol{v}}_p)$ is processed for SAR imaging.

$$y_t(t_r, t_a; \hat{\boldsymbol{v}}_p) = \text{IFFT}_a[y_e(t_r, f_a; \hat{\boldsymbol{v}}_p)] \quad (35)$$

$$y_{im}(x, y; \hat{\boldsymbol{v}}_p) =$$
$$\int_{t_a} y_t\left(\frac{\hat{R}(t_a; x, y, \hat{\boldsymbol{v}}_p)}{c}, t_a; \hat{\boldsymbol{v}}_p\right) \exp\left\{j\frac{2\pi}{\lambda}\hat{R}(t_a; x, y, \hat{\boldsymbol{v}}_p)\right\} dt_a \quad (36)$$

where $\text{IFFT}_a[\cdot]$ is the azimuthal inverse Fourier transform, and $\hat{R}(t_a; x, y, \hat{\boldsymbol{v}}_p)$ is the bistatic slant range calculated using (1) based on the grid position (x, y), the radar position, and the assumed target velocity $\hat{\boldsymbol{v}}_p$. Traversing different $\hat{\boldsymbol{v}}_p$, CFAR detection is performed on the response $|y_{im}(x, y; \hat{\boldsymbol{v}}_p)|$ for detecting moving targets.

The efficiency of the GEO SA-BSAR MTI processing can be characterized by the improvement factor, which is defined as the ratio of the SNRs at the input and the output

$$\text{IF} = \frac{P_s^{\text{out}}/P_n^{\text{out}}}{P_s^{\text{in}}/P_n^{\text{in}}} = \frac{y_{im}^* y_{im}/(y_{im,c}^* y_{im,c})}{P_s^{\text{in}}/P_n^{\text{in}}} \quad (37)$$

where $y_{im,c}$ is the output response of the interference. Since the derivation of (36) is complex, the impact of nonideal factors such as synchronization error and GEO orbit error on the final output response is analyzed using simulation.

For the synchronization error, we consider a high-stability quartz crystal with a fixed frequency deviation of 12.5 Hz and a linear time-synchronization error coefficient α of 10^{-8}. This time-synchronization error produces an offset of the Doppler center frequency αf_c of 12.5 Hz with a wavelength of 0.24 m. Then, the time and frequency synchronization errors together produce a Doppler center frequency shift of 25 Hz. For the GEO orbital error, the orbit of the Beidou IGSO satellite, which has a similar orbit to the GEO SAR, is used as a reference, and the broadcast ephemeris of the measured Beidou IGSO satellite (C06, Time: Mar. 22, 2022) is used as the real-time acquired satellite orbital position, while the precision ephemeris after 7
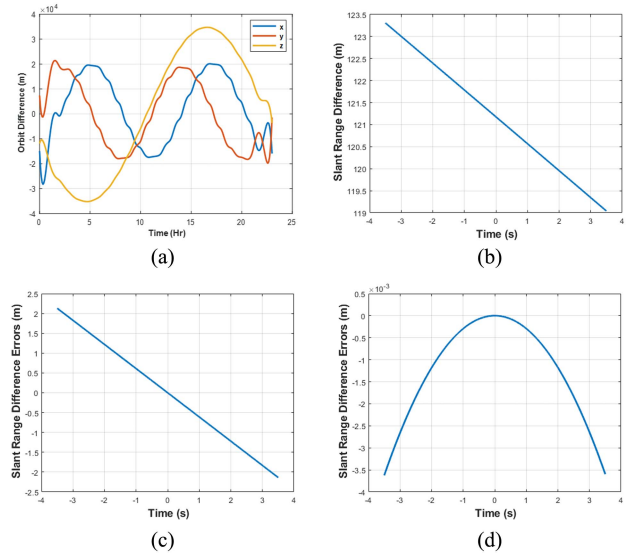

Fig. 2. Comparison between the broadcast and the precise ephemeris of an IGSO satellite (C06, Time: Mar. 22, 2022) [29]: (a) the orbit difference; (b) the slant range difference of the signal direct; the slant range difference errors of (c) constant approximation; and (d) linear approximation.
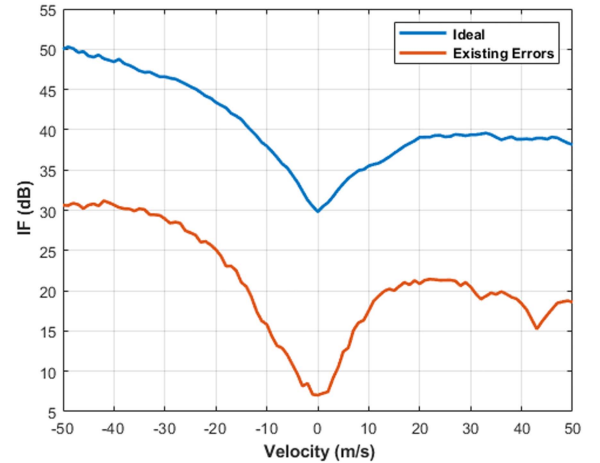

Fig. 3. Improvement factors under ideal situation and nonideal factors.

days is used as the satellite's real orbital position for simulation [29]. The orbit errors can be seen in Fig. 2.

The improvement factors for the ideal situation and with nonideal factors are shown in Fig. 3. The simulated parameters are shown in Table I. Ideally, moving targets have a high signal-to-noise gain, which is produced by the combined impact of the MTI processor $\mathbf{w}(f_a; \hat{\boldsymbol{v}}_p)$ suppression of clutter and the imaging processing focusing on the moving target energy. When there are synchronization errors and GEO orbit errors, on the one hand, the constructed MTI processor $\mathbf{w}(f_a; \hat{\boldsymbol{v}}_p)$ is mismatched with the motion target echo signal, and on the other hand, the imaging processing cannot accurately compensate for the phase of the motion target signal resulting in target defocusing, which ultimately leads to a significant decrease in the SNR gain. It can be seen that the combined impact of synchronization error and GEO orbit error significantly reduces the processed SNR gain, leading to more difficult detection of weak targets.

TABLE I
GEO SA-BSAR MTI SYSTEM PARAMETERS

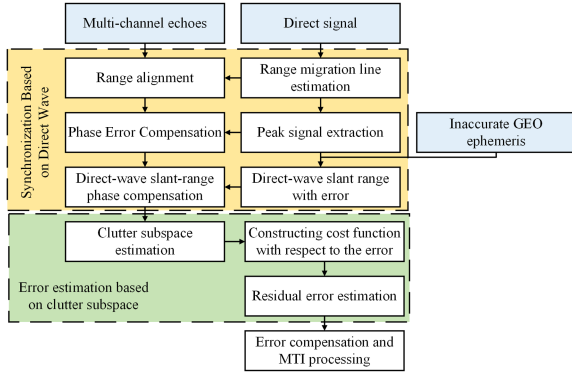| Receiver system parameters		Bistatic configuration parameters	
Wavelength	0.24 m	Angle of incidence of aircraft	30°
Bandwidth	60 MHz		
Receiver's height	3 km	Ground projection of bistatic Angle	0°
Receiver's speed	100 m/s		
Antenna Size	1.2 m	Ground projection of velocity Angle	0°

Fig. 4. Flowchart of GEO SA-BSAR synchronization and MTI scheme based on direct wave phase and clutter subspace.

III. GEO SA-BSAR SYNCHRONIZATION AND MTI METHOD BASED ON DIRECT SIGNAL AND CLUTTER SUBSPACE

This section discusses in detail the GEO SA-BSAR synchronization and MTI methods in the presence of synchronization errors and GEO orbit errors. The flowchart of the proposed method is shown in Fig. 4.

First, the signal is preprocessed to remove time and phase synchronization errors by range alignment and phase compensation of the echo signal using the migrating line of the direct signal and the phase of its peak signal, respectively. Next, the stationary clutter in the scene is used as an auxiliary calibration source. The covariance matrix of the clutter is estimated from the stationary clutter, and the clutter subspace is obtained by eigenvalue decomposition. Then, the cost function is formulated using the clutter steering vector parallel to the clutter subspace, and the residual error is estimated by minimizing it. Finally, a new processor is presented to compensate for residual errors and MTI. The exact process is detailed below.

A. Direct-Signal-Based GEO SA-BSAR Synchronization

The synchronization based on direct signal includes echo rearranging, range migration compensation, and phase compensation. First, 1-D echo can be rearranged into several pulses of f_s/PRF samples in which f_s is the sampling rate and PRF is the pulse-repetition frequency. The PRF is coarse and can be calculated according to the main-lobe position of the direct signal. Then, the rearranged echo and direct signal are range

compressed. Under the influence of time and frequency synchronization errors, the range-compressed direct signal can be expressed as

$$s_d^{rc}(r, t_a) = \omega_a(t_a) \, \text{sinc} \left[r + c \cdot e(t_a) - R_d(t_a) \right]$$
$$\exp\left\{ -j\Delta\varphi_{bi}(t_a) \right\} \exp\left\{ j2\pi f_c \left[e(t_a) - \frac{R_d(t_a)}{c} \right] \right\}. \quad (38)$$

The range migration line is

$$R_{rm}(t_a) = R_d(t_a) - c \cdot e(t_a) + \varepsilon_R(t_a) \quad (39)$$

where $\varepsilon_R(t_a)$ is the range migration line estimation error. It can be seen that it is mainly affected by the time synchronization error. The time synchronization error compensation function in the range frequency domain is constructed as

$$h_e(f_r, t_a) = \exp\left\{ j2\pi f_r \frac{R_{rm}(t_a)}{c} \right\}. \quad (40)$$

The phase at the peak of the direct signal is extracted to construct the compensation function for the frequency synchronization error

$$h_f(t_a) = \exp\left\{ -j \cdot \text{Angle}\left[s_d^{rc}(c \cdot R_{rm}(t_a), t_a) \right] \right\} \quad (41)$$

where Angle[·] returns the signal's phase. After multiplying the pulse-compressed echo in the range-frequency domain with $h_e(f_r, t_a)$ and $h_f(t_a)$, respectively, and inverse Fourier transforming it back to the time domain, the resulting echo signal of the mth channel can be expressed as

$$s_m(r, t_a) = \text{sinc}\left[r - R_{bi,m}(t_a) + R_d(t_a) + \varepsilon_R(t_a) \right]$$
$$\cdot \sigma_t \omega_a(t_a) \exp\left\{ -j2\pi f_c \frac{R_{bi,m}(t_a) - R_d(t_a)}{c} \right\}. \quad (42)$$

So far, the time and frequency synchronization errors are compensated, but the slant range history becomes $R_{bi,m}(t_a) - R_d(t_a)$, which makes the motion target detection process more complicated. Using the imprecise GEO ephemeris, it is possible to compute the slant range history $\tilde{R}_d(t_a)$ of the direct signal containing the error and accordingly construct the phase compensation function in the range frequency domain

$$h_{com} = \exp\left\{ j2\pi(f_r + f_c) \frac{\tilde{R}_d(t_a)}{c} \right\}. \quad (43)$$

The echo of the mth channel after compensation can be expressed as

$$s_m(r, t_a) = \text{sinc}\left[r - R_{bi,m}(t_a) + \Delta R_d(t_a) + \varepsilon_R(t_a) \right]$$
$$\cdot \sigma_t \omega_a(t_a) \exp\left\{ -j2\pi f_c \frac{R_{bi,m}(t_a) - \Delta R_d(t_a)}{c} \right\} \quad (44)$$

where $\Delta R_d(t_a)$ is the residual error arising from the imprecise GEO ephemeris, modeled as a polynomial

$$\Delta R_d(t_a) = \Delta R_{d0} + \Delta k_1 t_a + \cdots \quad (45)$$

where the constant term ΔR_{d0} only changes the range across the SAR image and does not change the relative position of

the moving target to the SAR background image, so it is not corrected here. In addition, the linear term error produces a Doppler center shift that affects target parameter estimation and target focusing, leading to increased noise and weakening target detection. By analyzing actual broadcast ephemerides and precision ephemerides, as shown in Fig. 2(c) and (d), the errors of the higher order terms of the residual error over shorter aperture times is less than $\lambda/16$ and will not affect the target focusing. Thus, the higher order terms can be negligible.

B. Error Estimation Based on Clutter Subspace

The echo after compensation in the previous section has only one residual linear phase error, and by transforming it to the range-Doppler domain, the multichannel signal model of a stationary target containing the residual error can be expressed as

$$z_c\,(r, f_a) = \tilde{S}_c\,(r, f_a)\,\Gamma_\varepsilon p_c\,(f_a) \tag{46}$$

where $\tilde{S}_c(r, f_a)$ is the range-Doppler domain signal of the reference channel after compensation in the previous section, and

$$\Gamma_\varepsilon = \mathrm{diag}\left\{1, \exp\left(-j2\pi\frac{\Delta k_1 d}{\lambda v_R}\right), \ldots, \exp\left(-j2\pi\frac{\Delta k_1 (M-1)d}{\lambda v_R}\right)\right\}. \tag{47}$$

The covariance matrix $\mathbf{R_Q}$ of the stationary clutter estimated from the observed data

$$\boldsymbol{R_Q}\,(f_a) = \frac{1}{N_r}\sum_{l=r}^{r+N_r-1} \boldsymbol{z}_c\,(l, f_a)\,\boldsymbol{z}_c(l, f_a)^H \tag{48}$$

where N_r is the number of range cells used to estimate the covariance matrix. The eigenvalue decomposition of the covariance matrix $\mathbf{R_Q}$ of the clutter is performed to obtain

$$\boldsymbol{R_Q} = \sum_{m=1}^{M}\lambda_m \boldsymbol{u}_m \boldsymbol{u}_m^H \tag{49}$$

where λ_m is the eigenvalue of $\mathbf{R_Q}$ satisfying $\lambda_1 \gg \lambda_2 = \cdots = \lambda_M = \sigma_n^2$ [30] and $\boldsymbol{u}_m$ is the eigenvector of $\mathbf{R_Q}$. $\boldsymbol{u}_1$ represents the clutter subspace and $\mathbf{U}^\perp = [\boldsymbol{u}_2, \cdots, \boldsymbol{u}_M]$ constitutes the orthogonal complementary space of the clutter subspace. Analytic derivation yields an expression for the clutter subspace as

$$\boldsymbol{u}_1 = E\left[\tilde{S}_c\,(r, f_a)\,\tilde{S}_c^*\,(r, f_a)\right]\begin{bmatrix}1 \\ e^{j\frac{2\pi d}{v_R}\left(f_a+\frac{s_{1c}-\Delta k_1}{\lambda}\right)} \\ \vdots \\ e^{j\frac{2\pi d}{v_R}\left(f_a+\frac{s_{1c}-\Delta k_1}{\lambda}\right)(M-1)}\end{bmatrix}. \tag{50}$$

The clutter subspace can be seen to contain the error Δk_1 introduced by the imprecise GEO orbit. In addition, s_{1c} is related to the GEO orbit and cannot be obtained from precise calculations. Next, we define a cost function based on the clutter subspace for iteratively estimating the unknown error. Define the

cost function as

$$J = \int \|(\boldsymbol{U}^\perp)^H \tilde{\boldsymbol{p}}_c\,(f_a)\|df_a \tag{51}$$

where

$$\tilde{\boldsymbol{p}}_c\,(f_a) = \begin{bmatrix}1 & e^{j\frac{2\pi d}{v_R}(f_a+\Delta\tilde{f})} & \cdots & e^{j\frac{2\pi d}{v_R}(f_a+\Delta\tilde{f})(M-1)}\end{bmatrix}^T \tag{52}$$

where $\Delta\tilde{f}$ is the residual error to be estimated, iterates over all possible $\Delta\tilde{f}$ to find the one that minimizes the cost function J. The estimated obtained $\Delta\tilde{f}$ will be used in the following section for the MTI processing.

C. Error Compensation and MTI Processing

This section describes the MTI processing in detail. First, the echoes are transformed to the range-Doppler domain, and the signal models for moving and stationary targets are shown in (23) and (26), respectively. Then, the signals in range-Doppler domain are used for MTI processing. Due to the problems of synchronization and GEO orbit inaccuracies, the signals contain residual errors that require reconstruction of the processor weight vectors for MTI

$$\boldsymbol{w}_{\mathrm{new}}\,(f_a; \widehat{\boldsymbol{v}}_p) = \frac{\boldsymbol{R_Q}^{-1}\,(f_a)\,\Gamma_f \hat{\boldsymbol{p}}_t\,(f_a; \widehat{\boldsymbol{v}}_p)}{\hat{\boldsymbol{p}}_t^H\,(f_a; \widehat{\boldsymbol{v}}_p)\,\Gamma_f^H \boldsymbol{R_Q}^{-1}\,(f_a)\,\Gamma_f \hat{\boldsymbol{p}}_t\,(f_a; \widehat{\boldsymbol{v}}_p)} \tag{53}$$

where

$$\Gamma_f = \mathrm{diag} \\ \times\left\{e^{-j2\pi\left(\Delta\hat{f}-\frac{\widehat{\boldsymbol{v}}_T^T\widehat{\boldsymbol{T}}_0}{\lambda\|\widehat{\boldsymbol{T}}_0\|}\right)\Delta t_{0,1}}, \ldots, e^{-j2\pi\left(\Delta\hat{f}-\frac{\widehat{\boldsymbol{v}}_T^T\widehat{\boldsymbol{T}}_0}{\lambda\|\widehat{\boldsymbol{T}}_0\|}\right)\Delta t_{0,M}}\right\}. \tag{54}$$

The improved MTI processor (53) adds a compensation factor Γ_f compared to the conventional MTI processor (29), which is used to compensate for the residual error after synchronization based on direct signal. Next, a new imaging process is performed on the output response $y(t_r, f_a; \widehat{\boldsymbol{v}}_p)$ of the MTI processor. The output response is transformed to the 2-D time domain and the moving target is focused according to the residual error and target slant range history

$$y_t\,(t_r, t_a; \widehat{\boldsymbol{v}}_p) = \mathrm{IFFT}_a\,[y\,(t_r, f_a; \widehat{\boldsymbol{v}}_p)] \tag{55}$$

$$y_{im}\,(x, y; \widehat{\boldsymbol{v}}_p) = \\ \int_{t_a} y_t\left(\frac{1}{c}\left[\hat{R}\,(t_a; x, y, \widehat{\boldsymbol{v}}_p)+\lambda\left(\Delta\hat{f}-\frac{\widehat{\boldsymbol{v}}_T^T\hat{\boldsymbol{T}}_0}{\lambda\|\hat{\boldsymbol{T}}\|_0}\right)\cdot t_a\right], t_a; \widehat{\boldsymbol{v}}_p\right) \\ \exp\left\{j\frac{2\pi}{\lambda}\left[\hat{R}\,(t_a; x, y, \widehat{\boldsymbol{v}}_p) + \lambda\left(\Delta\hat{f}-\frac{\widehat{\boldsymbol{v}}_T^T\hat{\boldsymbol{T}}_0}{\lambda\|\hat{\boldsymbol{T}}_0\|}\right)\cdot t_a\right]\right\}dt_a \tag{56}$$

where $\mathrm{IFFT}_a[\cdot]$ is the azimuthal inverse Fourier transform and $\hat{R}(t_a; x, y, \widehat{\boldsymbol{v}}_p)$ is the bistatic slant range history calculated using (1) according to the grid position (x, y), the radar position, and the assumed target velocity $\widehat{\boldsymbol{v}}_p$. $\lambda(\Delta\hat{f}-\widehat{\boldsymbol{v}}_T^T\hat{\boldsymbol{T}}_0/\lambda\|\hat{\boldsymbol{T}}_0\|)\cdot t_a$ was

TABLE II
PARAMETERS OF HIGH STABILITY QUARTZ CRYSTAL FREQUENCY SOURCE FOR SIMULATION

Parameters		Value
Center frequency		10 MHz
Frequency accuracy		$10^{-8} \sim 10^{-10}$
Frequency stability		$1 \times 10^{-12} \sim 3 \times 10^{-11}$
Time synchronization error parameters	Fixed-time deviation	1 ns
	Linear time synchronization error	10^{-8}
	Standard deviation of random errors	3×10^{-11}
Frequency synchronization error parameters	Fixed frequency deviation	12.5 Hz
	Power spectral coefficient of phase noise	b0 (dBc/Hz) -160
		b1 (dBc) -140
		b2 (dBc·Hz) -200
		b3 (dBc·Hz2) -100
		b4 (dBc·Hz3) -100

used to compensate for inaccurate GEO position errors. Finally, traversing different $\widehat{\mathbf{v}}_p$, CFAR detection is performed on the response $|y_{im}(x, y, \widehat{\mathbf{v}}_p)|$. For a detected target, the corresponding $\widehat{\mathbf{v}}_p$ is the estimated target motion parameter.

IV. SIMULATION EXPERIMENT ANALYSIS

In this section, the effectiveness of the proposed synchronization MTI method is demonstrated using simulation experiments. The bistatic parameters of the GEO SA-BSAR system are shown in Table I. Time and frequency synchronization errors all stem from inaccuracies and instabilities in the frequency source. For the highly stable quartz crystal frequency source, its typical frequency accuracy and frequency stability are shown in Table II, and the parameters of time and frequency synchronization errors are given accordingly. For the time synchronization error, it is assumed that the fixed time deviation is 1 ns. Its linear error is related to the frequency accuracy, which is set to 10^{-8}. The random error obeys a Gaussian distribution with a mean of 0, and its standard deviation is related to the frequency stability, which is set to 3×10^{-11}. For the frequency synchronization error, the fixed frequency deviation is related to the frequency accuracy and is set to $10^{-8} f_c$, and the phase noise is generated according to the power-law power spectrum [19].

Parameters in Table II were used to simulate time and phase synchronization errors, as depicted in Fig. 5. The results reveal that linear terms dominate the time and frequency synchronization errors. The linear term coefficient α of the time synchronization error obtained by fitting is 10^{-8}, and the offset of the
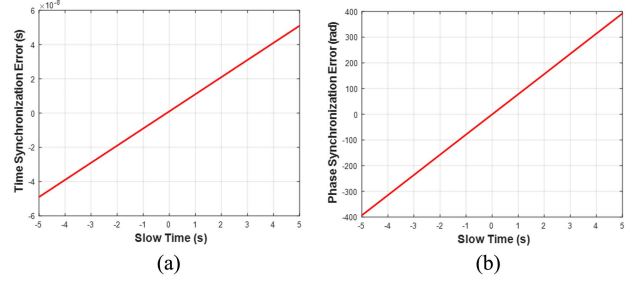

Fig. 5. Synchronization Error Simulation. (a) Time synchronization error. (b) Phase errors from frequency synchronization errors.
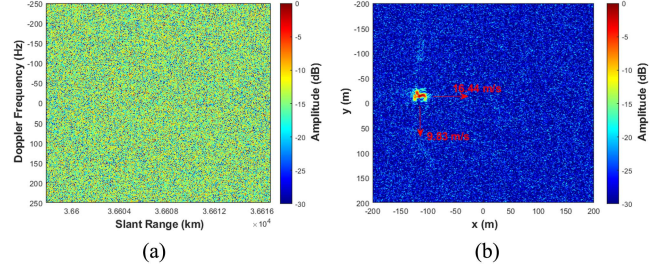

Fig. 6. Point-target simulation results. (a) RD-domain signal. (b) MTI processing result without error compensation.

Doppler center frequency produced by this time delay is αf_c of 12.500 Hz. The linear term coefficient of the phase error resulting from the frequency synchronization error obtained from the fit is 78.52 rad/s, which corresponds to a Doppler center frequency error of 12.497 Hz. In summary, the time and frequency synchronization errors together produce a Doppler center frequency shift of 24.997 Hz.

A. Point Target Simulation Verification

In this section, simulations of point targets are carried out to show the effects of synchronization errors and inaccurate GEO position on the signal processing, and to verify the effectiveness of the proposed method for MTI under nonideal factors. A moving target with a position of $(0, 0, 0)^T$ m and a velocity vector of $(10, 10, 0)^T$ m/s is set up in the imaging scene of the GEO SA-BSAR, and the background clutter is set to be uniform and obeying a Gaussian distribution. The echo signal in the range-Doppler domain is shown in Fig. 6(a), at which point the SCR is -1.5 dB, and the target is completely submerged in clutter, making it impossible to observe the moving target. MTI processing and imaging were performed directly on the echo signal, and the results obtained are shown in Fig. 6(b). The synchronization errors and the imprecise position of the GEO lead to the target not being fully focused, resulting in a loss of SNR. In addition, the parameter estimation result is $(16.34, 8.85, 0)^T$ m/s, which is a large difference from the true value. The target focus position deviates significantly from the actual position. Thus, the results are unsuitable for credible target detection and parameter estimation.

Next, the synchronization and error estimation process based on direct wave and clutter subspace is performed. By minimizing the cost function, the residual error is estimated, as shown in

TABLE III
RESIDUAL ERROR ESTIMATION RESULTS

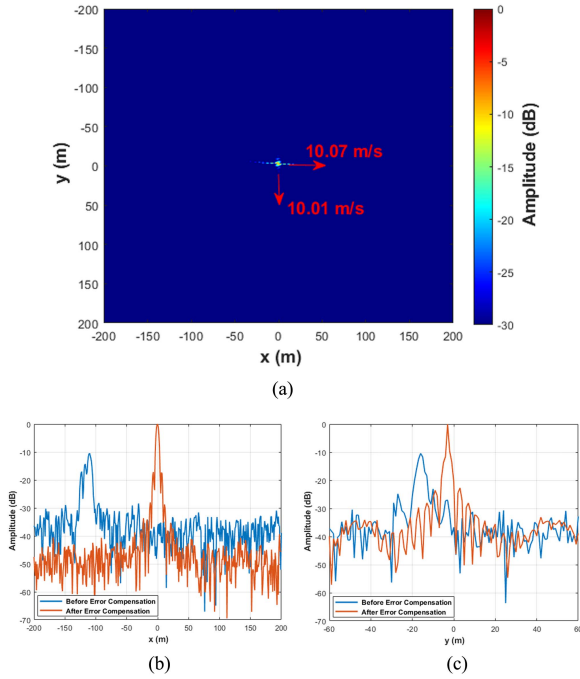| Estimated value $\Delta\hat{f}$	Truth value	Estimation error
-30.670 Hz	-30.668 Hz	0.002 Hz

(a)

(b)   (c)

Fig. 7. Results after the proposed processing. (a) Target imaging results and parameter estimation results. (b) x-direction profiles before and after error compensation. (c) y-direction profiles before and after error compensation.

TABLE IV
POINT TARGET PARAMETER ESTIMATION RESULTS

	Estimated value	Truth value	Estimation error
Position x	0 m	0 m	0 m
Position y	-3 m	0 m	3 m
Velocity v_x	10.07 m/s	10 m/s	0.07 m/s
Velocity v_y	10.01 m/s	10 m/s	0.01 m/s

Table III, with an error of only 0.002 Hz. Finally, the MTI and imaging processes are conducted, and the target velocity that maximizes the output energy is obtained using Bayesian optimization. The target is imaged using this velocity, and the results are shown in Fig. 7(a). The target is brought into full focus while positioned at the center of the scene and the speed is accurately estimated. Fig. 7(b) and (c) shows the profiles of the target imaging results before and after the error compensation, respectively. It can be seen that the target energy is improved by 10 dB after the error compensation, which is favorable for the detection of weak targets. The specific estimates of the target parameters are shown in Table IV, and the localization error of the target at this point does not exceed 5 m, and the velocity estimation error does not exceed 0.1 m.

Furthermore, the improvement factor is utilized to illustrate the efficiency of the proposed method, as shown in Fig. 8.
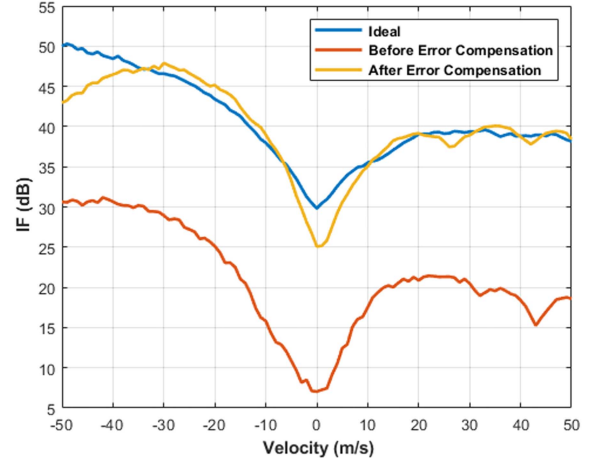

Fig. 8. Comparison of improvement factor results.

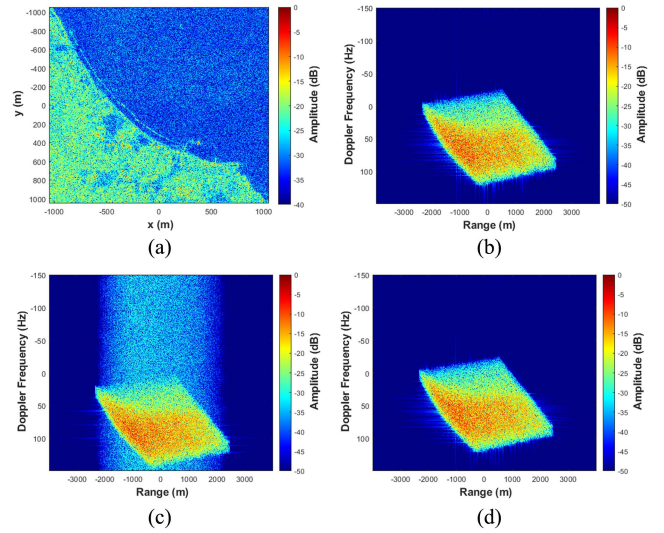(a)   (b)

(c)   (d)

Fig. 9. Signal processing results. (a) Original SAR image. (b) Ideal signal in range-Doppler domain. (c) Range-Doppler signals with time and frequency synchronization errors. (d) Range-Doppler signal after being processed by the proposed method.

Comparing the conventional GEO SA-BSAR MTI method, the proposed method has a better match with the desired improvement factors and has a better efficiency.

B. Simulation Verification Based on SAR Images

The background clutter of GEO SA-BSAR is generated using existing SAR images. The amplitude values of the SAR images of ALOS PALSAR are used as scattering coefficients to generate the multichannel echoes under the GEO SA-BSAR geometric relationship. Four moving targets were set up in the scene species, and the target speeds were set to 5 m/s or 8 m/s.

Fig. 9(a) and (b) shows the original SAR image and its range-Doppler signal, respectively. Fig. 9(c) shows the range-Doppler signals with time and frequency synchronization errors. When there are errors, the Doppler center frequency appears to be shifted, and the azimuthal spectrum appears to be broadened by phase noise. There is also strong signal energy beyond the main
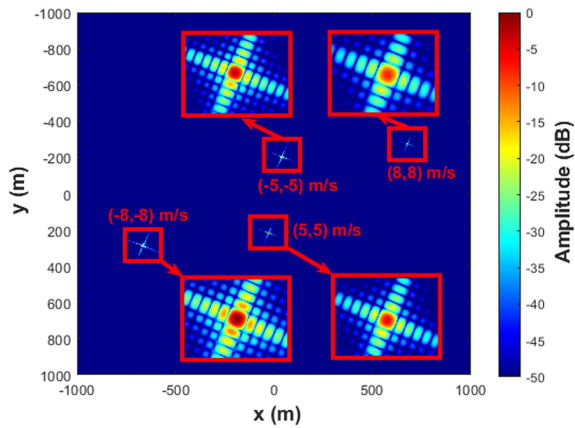
Fig. 10. Motion target imaging results.

lobe of the clutter. Then, the errors arising from nonideal factors are estimated and compensated using the method proposed in this article based on direct wave and clutter subspace. It should be noted that the number of range units used to estimate the clutter covariance matrix in this method is 200. The compensated range-Doppler signal is shown in Fig. 9(d), where it can be seen that the spectral spreading and offset generated by the nonideal error are compensated. Finally, the results of motion target imaging and parameter estimation are shown in Fig. 10, where the target is well-focused and the motion parameters are accurately estimated.

V. CONCLUSION

The GEO SA-BSAR system uses different frequency sources at the receiver and transmitter, resulting in time and frequency synchronization errors. In addition, the high GEO SAR orbit leads to poor orbiting accuracy, which introduces a residual error in synchronization processing. The residual error reduces the SNR and leads to parameter estimation errors, resulting in difficulties in weak target detection. In this article, a synchronization and MTI method based on direct signal and clutter subspace is proposed, which can achieve high output SNR in the absence of the accurate GEO position. Since there is no on-orbit GEO SAR yet, this article carries out semiphysical simulation experiments based on typical high-stability quartz crystal oscillator parameters, IGSO orbital, and SAR image data to verify the effectiveness of the proposed algorithm. The proposed method greatly improves the output SNR (by about 10 dB), and the velocity estimation error is less than 0.1 m/s.

REFERENCES

[1] G. L. Guttrich, W. E. Sievers, and N. M. Tomljanovich, "Wide area surveillance concepts based on geosynchronous illumination and bistatic unmanned airborne vehicles or satellite reception," in *Proc. IEEE Nat. Radar Conf.*, 1997, pp. 126–131.

[2] S. Ghaleb and A. K. Floyd, "Method of using a microwave and millimeter frequency bistatic radar for tracking and fire control," U.S. Patent 7 710 313, May 4, 2010.

[3] H. Y. Shi, Y. Q. Zhou, and J. Chen, "An algorithm of geo spaceborne-airborne bistatic three-channel SAR ground moving target indication," *J. Electron. Inf. Technol.*, vol. 12, 2009, Art. no. 1810.

[4] H. An, J. Wu, K. C. Teh, Z. Sun, and J. Yang, "Simultaneous moving and stationary target imaging for geosynchronous spaceborne-airborne bistatic SAR Based on sparse separation," *IEEE Trans. Geosci. Remote Sens.*, vol. 59, no. 8, pp. 6722–6735, Aug. 2021, doi: 10.1109/TGRS.2020.3025802.

[5] X. Dong, C. Cui, Y. Li, and C. Hu, "Geosynchronous spaceborne-airborne bistatic moving target indication system: Performance analysis and configuration design," *Remote Sens.*, vol. 12, no. 11, 2020, Art. no. 8150, doi: 10.3390/rs12111810.

[6] G. Li, J. Xu, Y. Peng, and X. Xia, "Bistatic linear antenna array SAR for moving target detection, location, and imaging with two passive airborne radars," *IEEE Trans. Geosci. Remote Sens.*, vol. 45, no. 3, pp. 554–565, Mar. 2007, doi: 10.1109/TGRS.2006.888145.

[7] Y. Zhang, W. Xiong, X. Dong, and C. Hu, "A novel azimuth spectrum reconstruction and imaging method for moving targets in geosynchronous spaceborne–airborne bistatic multichannel SAR," *IEEE Trans. Geosci. Remote Sens.*, vol. 58, no. 8, pp. 5976–5991, Aug. 2020, doi: 10.1109/TGRS.2020.2974531.

[8] W. Xu et al., "Azimuth multichannel reconstruction for moving targets in geosynchronous spaceborne-airborne bistatic SAR," *Remote Sens.*, vol. 12, no. 11, 2020, Art. no. 1703, doi: 10.3390/rs12111703.

[9] C. Cui, X. Dong, Z. Chen, C. Hu, and W. Tian, "A long-time coherent integration STAP for GEO spaceborne-airborne bistatic SAR," *Remote Sens.*, vol. 14, no. 3, 2022, Art. no. 1706, doi: 10.3390/rs14030593.

[10] C. Cui, X. Dong, Y. Li, Z. Chen, and X. Li, "DNN with similarity constraint for GEO SA-BSAR moving target imaging," *IEEE Geosci. Remote Sens. Lett.*, vol. 19, 2022, Art. no. 4512005, doi: 10.1109/LGRS.2022.3196674.

[11] L. Ling, Z. Yinqing, J. Li, and S. Bing, "Synchronization of geo spaceborne-airborne bistatic SAR," in *Proc. IEEE Int. Geosci. Remote Sens. Symp.*, 2008, pp. III-1209–III-1211, doi: 10.1109/IGARSS.2008.4779574.

[12] D. Liang, H. Zhang, K. Liu, D. Liu, and R. Wang, "Phase synchronization techniques for bistatic and multistatic synthetic aperture radar: Accounting for frequency offset," *IEEE Geosci. Remote Sens. Mag.*, vol. 10, no. 3, pp. 153–167, Mar. 2022, doi: 10.1109/MGRS.2022.3189005.

[13] M. Weib, "Synchronisation of bistatic radar systems," in *Proc. IEEE Int. Geosci. Remote Sens. Symp.*, 2004, pp. 1750–1753, doi: 10.1109/IGARSS.2004.1370671.

[14] G. Jin et al., "An advanced phase synchronization scheme for LT-1," *IEEE Trans. Geosci. Remote Sens.*, vol. 58, no. 3, pp. 1735–1746, Mar. 2020, doi: 10.1109/TGRS.2019.2948219.

[15] D. Liang et al., "A high-accuracy synchronization phase-compensation method based on kalman filter for bistatic synthetic aperture radar," *IEEE Geosci. Remote Sens. Lett.*, vol. 17, no. 10, pp. 1722–1726, Oct. 2020, doi: 10.1109/LGRS.2019.2952475.

[16] G. Krieger et al., "TanDEM-X: A radar interferometer with two formation-flying satellites," *Acta Astronautica*, vol. 89, pp. 83–98, Aug. 2013.

[17] Y. Jiao, D. Liang, K. Liu, Y. Chen, H. Wang, and R. Wang, "The synchronization transceiver design and experimental verification for the LuTan-1 SAR satellite," *Sensors*, vol. 20, no. 5, 2020, Art. no. 1463.

[18] M. Rodriguez-Cassola, S. V. Baumgartner, G. Krieger, and A. Moreira, "Bistatic TerraSAR-X/F-SAR spaceborne–airborne SAR experiment: Description, data processing, and results," *IEEE Trans. Geosci. Remote Sens.*, vol. 48, no. 2, pp. 781–794, Feb. 2010, doi: 10.1109/TGRS.2009.2029984.

[19] P. Lopez-Dekker, J. J. Mallorqui, P. Serra-Morales, and J. Sanz-Marcos, "Phase synchronization and doppler centroid estimation in fixed receiver bistatic SAR systems," *IEEE Trans. Geosci. Remote Sens.*, vol. 46, no. 11, pp. 3459–3471, Nov. 2008, doi: 10.1109/TGRS.2008.923322.

[20] J. Sanz-Marcos, P. Lopez-Dekker, J. J. Mallorqui, A. Aguasca, and P. Prats, "SABRINA: A SAR bistatic receiver for interferometric applications," *IEEE Geosci. Remote Sens. Lett.*, vol. 4, no. 2, pp. 307–311, Apr. 2007, doi: 10.1109/LGRS.2007.894144.

[21] A. Hauschild, O. Montenbruck, P. Steigenberger, I. Martini, and I. Fernandez-Hernandez, "Orbit determination of sentinel-6A using the Galileo high accuracy service test signal," *GPS Solutions*, vol. 26, no. 4, Aug. 2022, Art. no. 120, doi: 10.1007/s10291-022-01312-5.

[22] S. C. Wu, T. P. Yunck, and C. L. Thornton, "Reduced-dynamic technique for precise orbit determination of low earth satellites," *J. Guid., Control, Dyn.*, vol. 14, no. 1, pp. 24–30, Jan. 1991, doi: 10.2514/3.20600.

[23] W. Bertiger et al., "GRACE: Millimeters and microns in orbit," in *Proc. 15th Int. Tech. Meeting Satell. Division Inst. Navigation (ION GPS 2002)*, Portland, OR, USA, Sep. 2002, pp. 2022–2029.

[24] S. B. Bisnath and R. B. Langley, "High-precision, kinematic positioning with a single GPS receiver," *Navigation*, vol. 49, no. 3, pp. 161–169, 2002.

[25] W. G. Melbourne, E. Davis, T. P. Yunck, and B. D. Tapley, "The GPS flight experiment on TOPEX/POSEIDON," *Geophysical Res. Lett.*, vol. 21, no. 19, pp. 2171–2174, 1994.

[26] J. Tombasco, *Orbit Estimation of Geosynchronous Objects Via Ground-Based and Space-Based Optical Tracking*. Boulder, CO, USA: Univ. of Colorado at Boulder, 2011.

[27] M. Zhang et al., "A synchronization algorithm for spaceborne/stationary BiSAR imaging based on contrast optimization with direct signal from radar satellite," *IEEE Trans. Geosci. Remote Sens.*, vol. 54, no. 4, pp. 1977–1989, Apr. 2016, doi: 10.1109/TGRS.2015.2493078.

[28] L. B. Fertig, "Analytical expressions for space-time adaptive processing (STAP) performance," *IEEE Trans. Aerosp. Electron. Syst.*, vol. 51, no. 1, pp. 42–53, Jan. 2015.

[29] I. G. S. (IGS), *GNSS Final Combined Clock Solution (5 Minute) Product*. Washington, DC, USA: NASA, 2022.

[30] D. Cerutti-Maori, I. Sikaneta, and C. H. Gierull, "Optimum SAR/GMTI processing and its application to the radar satellite RADARSAT-2 for traffic monitoring," *IEEE Trans. Geosci. Remote Sens.*, vol. 50, no. 10, pp. 3868–3881, Oct. 2012, doi: 10.1109/TGRS.2012.2186637.

Xichao Dong (Member, IEEE) received the B.S. degree in electrical engineering and the Ph.D. degree in target detection and recognition from the Beijing Institute of Technology (BIT), Beijing, China, in 2008 and 2014, respectively.

From 2011 to 2013, he was a Research Assistant with the Centre for Terrestrial Carbon Dynamics, University of Sheffield, Sheffield, U.K. From 2014 to 2017, he held a Postdoctoral position with the School of Information and Electronics, BIT. Since 2017, he has been an Assistant Professor with the School of Information and Electronics, BIT. Since 2019, he has been with the BIT Chongqing Innovation Center, Chongqing, China. His research interests include geosynchronous synthetic aperture radar and weather radar.

Dr. Dong was a recipient of the IEEE CIE International Radar Conference Excellent Paper Award in 2011 and the Chinese Institute of Electronics Youth Conference Poster Award in 2014.

Chang Cui was born in Hunan, China, in 1994. She received the B.S. degree in information engineering and Ph.D. degree in signal and infromation processing from the School of Information and Electronics, Beijing Institute of Technology, Beijing, China, in 2016 and 2022, respectively.

She is currently a Postdoctoral Researcher with the Beijing Institute of Technology Chongqing Innovation Center. Her research interests include geosynchronous synthetic aperture radar signal processing and moving target indication.

Zhiyang Chen (Member, IEEE) received the B.S. degree in electronic information science and technology from the Department of Electronic Engineering, Tsinghua University, Beijing, China, in 2016, and the Ph.D. degree in information and communication engineering from the School of Information and Electronics (SIE), Beijing Institute of Technology (BIT), Beijing, in 2021.

He has been an Assistant Professor in SIE, BIT, since 2024. His research interests include GEO SAR satellites formation design, SAR interferometry, and SAR tomography.

Dr. Chen was a recipient of the Best Paper Award in IET International Radar Conference 2023, and a recipient of Excellent Doctoral Thesis Award of GNSS and LBS Association of China.